

## **$4\pi$ studies of the 1.8–4.8 GeV $^3\text{He} + \text{natAg}$ , $^{197}\text{Au}$ reactions.**

### **II. Multifragmentation**

E. Renshaw Foxford, K. Kwiatkowski, D. S. Bracken, K. B. Morley, V. E. Viola, and N. R. Yoder

*Departments of Chemistry and Physics and Indiana University Cyclotron Facility, Indiana University, Bloomington, Indiana 47405*

C. Volant, E. C. Pollacco, and R. Legrain

*Commissariat à l'Energie Atomique, DAPNIA Service de Physique Nucléaire, C. E. Saclay, 91191 Gif-sur-Yvette, Cedex, France*

R. G. Korteling

*Department of Chemistry, Simon Fraser University, Burnaby, British Columbia, Canada*

W. A. Friedman

*Department of Physics, University of Wisconsin, Madison, Wisconsin 53706*

J. Brzychczyk

*Institute of Physics, Jagiellonian University, 30-059 Krakow, Poland*

H. Breuer

*Department of Physics, University of Maryland, College Park, Maryland 20742*

(Received 11 December 1995)

Multifragmentation of  $\text{natAg}$  and  $^{197}\text{Au}$  nuclei induced by 1.8–4.8 GeV  $^3\text{He}$  ions has been studied with the Indiana Silicon Sphere  $4\pi$  detector array. Rapidity, moving source, and sphericity-coplanarity analyses are consistent with near-simultaneous emission from a source in approximate kinetic equilibrium. For the most dissipative collisions, the spectral peaks are broadened and shifted to very low energies, indicative of emission from an extended nuclear system with  $\rho/\rho_0 \sim 1/3$ . Predictions of an intranuclear cascade/expanding, emitting source model compare well with experimental multiplicity distributions and the evolution of fragment spectral shapes. [S0556-2813(96)06208-5]

PACS number(s): 25.70.Pq, 21.65.+f, 25.55-e

#### **I. INTRODUCTION**

When nuclei are subjected to extreme conditions of thermal and/or compressional energy, multifragmentation occurs with high probability [1–4]. The nature of this disintegration process may provide insight into the nuclear equation of state (EOS) at low densities, limiting temperatures in the nuclear medium, and liquid-vapor phase coexistence in hot, finite nuclei [5–7]. Understanding the nuclear EOS is essential not only to account for the static and dynamic properties of finite nuclei, but also for describing astrophysical systems—for example, the aggregation of hadronic matter to form stars, and their subsequent evolution into supernovae, neutron stars, and black holes. In order to derive conclusions concerning the bulk properties of nuclear matter from experimental studies of the multifragmentation process, [8–17] several issues demand a higher level of understanding; e.g., reaction time scales, the excitation energy and degree of equilibration achieved in fragmenting systems, and the extent to which the final states are determined by phase space versus dynamics. A related important question is the role of nuclear expansion in the breakup process. Analysis of recent exclusive data [9,10,18–20] suggests that multifragmentation occurs from an extended nuclear system, corresponding to relatively low densities compared to normal nuclear matter density.

Investigations of hot nuclei formed with light-ion beams (H and He) at energies above  $\sim 1$  GeV are an important complement to studies with heavy-ion probes. For light-ion-

induced reactions, the multifragmentation mechanism is driven primarily by thermal heating and significantly influenced by the excitation of  $\Delta$  and higher resonances during the fast cascade, followed by rescattering and/or reabsorption of the decay pions [19,21,22]. The rapid evolution of such systems into regions of phase instability is indicated schematically in Fig. 1. Here the central collision trajectory ( $b = 1.8$  fm) is plotted for the 4.8 GeV  $^3\text{He} + \text{natAg}$  reaction in the phase diagram for infinite nuclear matter with  $Z/A = 0.4$ , as recently calculated by Müller and Serot [5]. The trajectory is based on Boltzmann-Uehling-Uhlenbeck (BUU) calculations for finite nuclei [23,24] and is traced in time steps of 4 fm/c in average entropy-per-nucleon versus density coordinates. Where the trajectory density refers to the maximum, rather than the average, nuclear density. The apparent compression that appears early in the dynamical evolution of the system is a reflection of the localized hadronic cascade that develops as the projectile momentum front passes through nucleus. Subsequently, the density is rapidly depleted by mass loss during the cascade and some expansion as the system cools along a constant entropy/nucleon path, entering the liquid-gas coexistence and spinodal instability regions on time scales of the order of 40 fm/c. Thus, these simulations suggest that light-ion-induced reactions provide an alternative probe of the equation of state for finite nuclear matter.

From a practical perspective, this rapid dissipation of energy permits separation of the collision and disassembly time

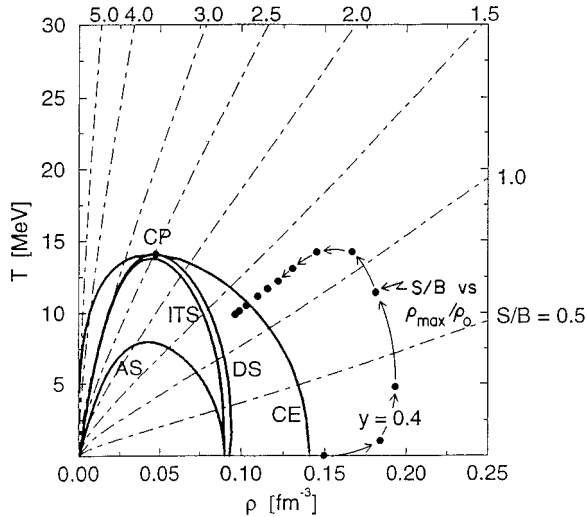


FIG. 1. Temperature-density phase diagram for infinite nuclear matter with  $y=Z/A=0.4$  from Müller and Serot [5]; entropy per baryon is indicated by dashed lines. Areas are defined as CE=liquid-gas coexistence, DS=diffusive spinodal, TS=isothermal spinodal, and AS=adiabatic spinodal. CP is the critical point. Reaction trajectory for the 4.8 GeV  ${}^3\text{He}+{}^{\text{nat}}\text{Ag}$  system [24] is plotted in average entropy ( $S/A$ ) versus maximum density ( $\rho_{\text{max}}/\rho_0$ ) coordinates in 4 fm/c time steps. The trajectory is for impact parameter  $b=1.8$  fm and is based upon BUU code of Danielewicz [23]. The apparent increase in density at early times reflects the localized effect of the projectile as it passes through the Ag nucleus.

scales, at least to first order. A further advantage of light-ion beams is that compressional and rotational effects should be small relative to heavy-ion collisions. Hence the thermal component of the multifragmentation process becomes more accessible to study. Finally, light-ion-induced reactions present the advantages of a single emitting source and complete, well-defined energy spectra with minimal distortion due to kinematic effects.

At present, few  $4\pi$  data exist for multifragmentation induced by light-ion beams. Early inclusive studies based on radiochemical, emulsion, and counter-telescope data (reviewed in Ref. [16]), provided evidence for a distinct mechanism change for fragment production when the bombarding energy exceeds about 1 GeV. The first counter studies with a large detector array were conducted by Warwick *et al.* [8], who measured low-energy complex fragments over a limited solid-angle range in conjunction with  $\sim 4\pi$  measurements of fast light charged particles in  $p$ -,  ${}^4\text{He}$ -, and  ${}^{20}\text{Ne}$ -induced reactions on heavy targets. Significant multiplicities of complex fragments were inferred from these measurements, which also suggested that the proton multiplicity might serve as a means for gauging the centrality of the reactions. More recently, Yennello *et al.* [9], performed limited exclusive measurements (8% or  $4\pi$ ) at 0.9 and 3.6 GeV on the  ${}^3\text{He}+{}^{\text{nat}}\text{Ag}$  system. This study showed a dramatic increase in the multiplicity of  $Z\geq 3$  fragments over this energy interval and also reported evidence for thermal expansion effects based on the character of the spectral peaks for high multiplicity events. In another recent  $4\pi$  study, Lips *et al.* [25] reported multiplicities for the  ${}^4\text{He}+{}^{197}\text{Au}$  system at 4.0 and 15 GeV that exceed those found in heavy-ion studies of simi-

lar systems. However, fragment identification was not possible in the experimental system used in Ref. [25], as discussed below.

In this paper, we report the first measurements of light-ion-induced multifragmentation in which both light-charged particles (LCP= $\text{H}$  and  $\text{He}$ ) and intermediate-mass fragments (IMF:  $3\leq Z\leq 20$ ) are fully  $Z$  identified with low thresholds and large solid angle coverage. The experiments were performed at the Saturne II accelerator at the Laboratoire National Saturne, Saclay, using the Indiana Silicon Sphere  $4\pi$  detector array [26]. We first discuss the probability for fragment formation and the properties of the emitting source as a function of deposition energy, and then consider the IMF charge distributions. Finally, we compare the data with precision of a hybrid intranuclear cascade/expanding emitting source model [2,19].

## II. EXPERIMENTAL RESULTS

Beams of 1.8, 3.6, and 4.8 GeV  ${}^3\text{He}$  ions were obtained from the Saturne II accelerator. LCP and IMF spectra from  ${}^{\text{nat}}\text{Ag}$  and  ${}^{197}\text{Au}$  targets were measured with the ISiS  $4\pi$  detector array, which contains 162 gas-ionization/0.5 mm silicon/28 mm CsI(Tl) detector telescopes, covering 74% of  $4\pi$ . The experimental details are described in the preceding paper [27]. In the following, we present results from the initial analyses of these data, as they relate to the multifragmentation process [28].

### A. Probability of IMF emission

One of the earliest indications that IMF emission is linked to highly excited nuclear matter was inferred from radiochemical excitation function measurements in light-ion-induced reactions [29–31]. These studies showed that IMF cross sections increase two to three orders of magnitude between bombarding energies of  $\sim 100$  MeV and about 10 GeV, above which they remain nearly constant out to 30 GeV [32].

Analogous behavior is observed for the  ${}^3\text{He}+{}^{\text{nat}}\text{Ag}$  system in Fig. 2 where the total IMF cross section (summed over  $3\leq Z\leq 16$ ) is plotted for each IMF multiplicity and bombarding energy between 200 MeV and 4.8 GeV. The 200 MeV data are taken from Ref. [33] and assume all IMF events are multiplicity one ( $M_{\text{IMF}}=1$ ); the 0.90 GeV data are based on Ref. [9]. The data of Ref. [9] have been renormalized to 0.78 times the quoted values in that work. This renormalization assumes a cross section of 43 mb for the  ${}^{12}\text{C}({}^3\text{He},x){}^{11}\text{C}$  monitor reaction [34], which is used to cross calibrate the secondary emission beam-intensity monitor [27]. This value replaces the value of 55 mb used earlier [35]. This new value is based on a systematic analysis of  ${}^{11}\text{C}$  cross sections for proton, deuteron, and alpha particle reactions on  ${}^{12}\text{C}$  over this energy range, which suggests the result of Ref. [35] may be anomalously high.

Cross sections for bombardments at 1.8, 3.6, and 4.8 GeV were based on the present measurements. Because of uncertainties in the absolute beam intensity and the fraction of the beam striking the  $6\times 6$  mm<sup>2</sup> target, the reaction cross sections,  $\sigma_R$ , were based on the predictions of Kox *et al.* [36], and Karol [37]. These calculations predict nearly identical

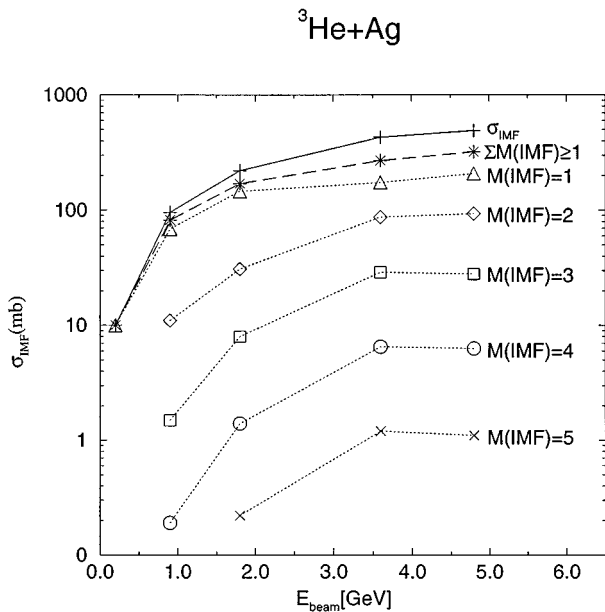


FIG. 2. Cross sections for IMF multiplicity  $M$  as a function of bombarding energy for the  ${}^3\text{He} + {}^{\text{nat}}\text{Ag}$  system. Data at 0.20 GeV are from Ref. [33] and those at 0.90 GeV are from Ref. [9]. Errors are statistical only; absolute errors are estimated to be of order  $\pm 20\%$ ; relative errors are much smaller.

values,  $\sigma_R = 1420$  mb for  ${}^3\text{He} + {}^{\text{nat}}\text{Ag}$  and  $\sigma_R = 1940$  mb for  ${}^3\text{He} + {}^{197}\text{Au}$  over the energy range 1.8 to 4.8 GeV. It is then assumed that when corrected for geometric acceptance, the ISiS array (trigger condition:  $\geq$  two charged particles) detects all events, except simple peripheral reactions. From the review of Hudis [38], it is estimated that events that emit fewer than two charged particles in the ISiS energy accep-

tance range account for about 100 mb of cross section in the Ag target and 150 mb in Au, independent of bombarding energy. Thus the total number of events in ISiS that meet the trigger condition,  $n(\text{ISiS})$ , is proportional to  $\sigma_{\text{total}} = 1320$  mb for  ${}^3\text{He} + {}^{\text{nat}}\text{Ag}$  and 1790 mb for  ${}^3\text{He} + {}^{197}\text{Au}$ . The total cross section for events with one or more IMF's is then given by

$$\sigma(M_{\text{IMF}} \geq 1) = [n(\text{IMF})/n(\text{ISiS})]\sigma_{\text{total}}, \quad (1)$$

where  $n(\text{IMF})/n(\text{ISiS})$  is the fraction of measured events that contains one or more IMF's.

The total IMF cross section for each multiplicity is determined from

$$\sigma(M_{\text{IMF}}) = [n(M_{\text{IMF}})/n(\text{ISiS})]\sigma_{\text{total}}, \quad (2)$$

where  $n(M_{\text{IMF}})$  is the number of IMF events of a given multiplicity. In order to obtain cross sections for each multiplicity,  $\sigma(M_{\text{IMF}})$ , absolute multiplicities are required. A simulation that includes detector geometry and experimental angular distributions has been performed with the program GEANT to generate reconstruction values of  $n(M_{\text{IMF}})$  from the measured distributions. Both the measured and reconstructed IMF multiplicity distributions are shown in Fig. 3. Here we define experimental multiplicities as  $N$  and reconstructed multiplicities as  $M$ .

From the total IMF cross sections and the reconstructed multiplicity distributions, it is then possible to obtain values of  $\sigma(M_{\text{IMF}})$ . Cross sections for multiplicity-dependent IMF emission, total events with  $M_{\text{IMF}} \geq 1$  and total inclusive IMF emission  $\sigma(M_{\text{IMF}})$  are given in Table I for both the  ${}^{\text{nat}}\text{Ag}$  and  ${}^{197}\text{Au}$  targets. We estimate the total error in these assumptions to be of order  $\pm 20\%$ ; the relative errors between individual multiplicities are considerably smaller. For the 3.6

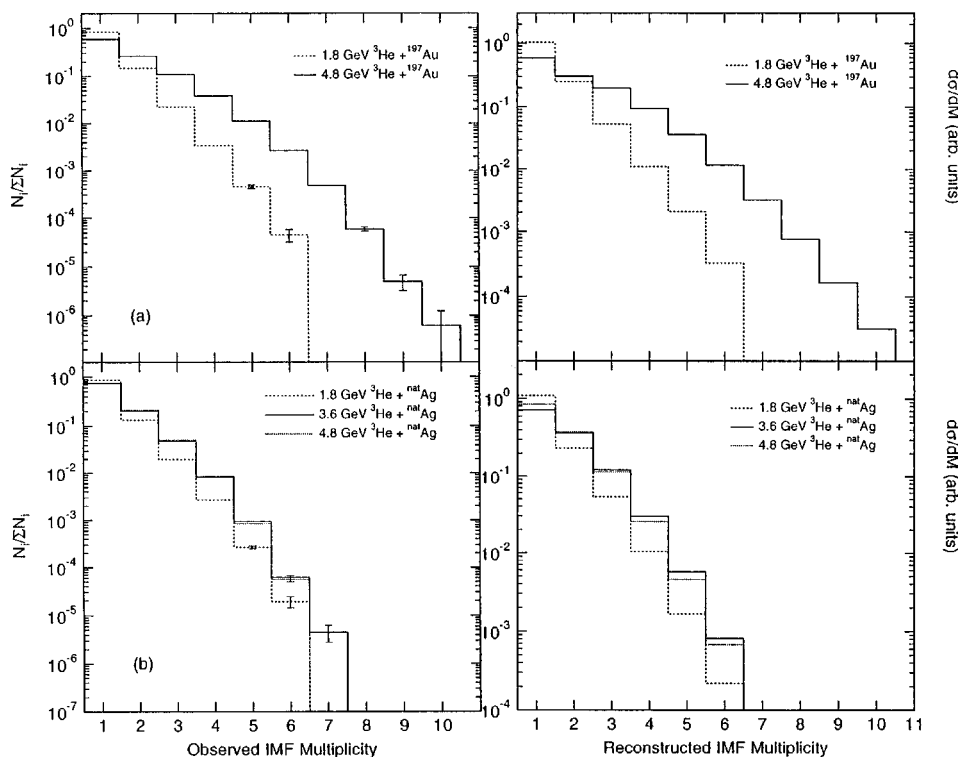


FIG. 3. Observed (left) and reconstructed (right) IMF multiplicity distributions for the 1.8 and 4.8 GeV  ${}^3\text{He} + {}^{197}\text{Au}$  reactions (top) and 1.8, 3.6, and 4.8 GeV  ${}^3\text{He} + {}^{\text{nat}}\text{Ag}$  reactions (bottom).

TABLE I. Cross section as a function of reconstructed multiplicity for IMF's emitted in  $^3\text{He}$ -induced reactions. Total cross sections for events in which one or more IMF's is emitted and the inclusive IMF cross sections are also tabulated. As described in text, systematic errors are estimated to be  $\pm 20\%$ ; relative errors are much smaller.

Energy (GeV)	$\sigma(M_{\text{IMF}})$ (mb)							
	$^3\text{He} + \text{natAg}$					$^3\text{He} + ^{197}\text{Au}$		
	0.2	0.9	1.8	3.6	4.8	1.8	4.8	4.8
1	10	69	140	160	190	270	300	
2		11	28	77	98	66	170	
3		1.5	7.4	26	28	14	110	
4		0.02	1.3	6.4	6.5	2.9	54	
5			0.2	1.2	1.2	0.5	20	
6			0.03	0.2	0.2	0.1	6.6	
7							1.8	
8							0.4	
9							0.1	
10							0.02	
$\sigma(M_{\text{total}})$ (mb)	10	82	170	270	320	350	660	
$\sigma_{\text{IMF}}$ (mb)	10	96	220	430	490	460	1320	

GeV  $^3\text{He} + \text{natAg}$  case, we find good agreement with the data of Ref. [9], as modified by the  $^{11}\text{C}$  cross section based on Ref. [34].

The excitation function for total IMF events (top curve in Fig. 2) illustrates the strong increase in IMF emission probability with increasing bombarding energy. The probability for high multiplicity events increases correspondingly between a projectile energy of 1 and 3 GeV. This behavior can be understood in terms of the enhanced deposition energy for central collisions provided by multiple nucleon-nucleon scatterings and the excitation and decay of  $\Delta$  resonances during the cascade, once the  $^3\text{He}$  energy exceeds the  $\Delta$  threshold [9,10]. The energy independence of the cross sections achieved above about 3 GeV has been interpreted in terms of a saturation in deposition energy that occurs when the projectile momentum front penetrates through the nucleus, as discussed in the previous paper [27].

The effect of target mass number is also apparent in comparing the results for  $\text{natAg}$  and  $^{197}\text{Au}$  at the same bombarding energy (Table I). At both 1.8 and 4.8 GeV, the IMF cross section for  $^{197}\text{Au}$  is about twice that for  $\text{natAg}$ . This presumably reflects the greater stopping power for the  $^{197}\text{Au}$  nucleus, as well as the larger cross sectional area for the central-density region.

Average reconstructed IMF multiplicities for events with at least one IMF are 1.3, 1.6, and 1.6 for the 1.8, 3.6, and 4.8 GeV  $^3\text{He} + \text{natAg}$  cases, and 1.3 and 2.0 for 1.8 and 4.8 GeV  $^3\text{He} + ^{197}\text{Au}$ , respectively. Errors are of the order of  $\pm 0.1$ . These multiplicities are comparable to, but slightly lower than, those measured for similar systems in heavy-ion-induced reactions [39–41] at comparable total energies. The value for the 4.8 GeV  $^3\text{He} + ^{197}\text{Au}$  system (2.0) is distinctly lower than the value of 3.8 recently reported for the 4.0 GeV  $^4\text{He} + ^{197}\text{Au}$  system [25], for which the predicted excitation energy distribution is quite similar to that for 4.8 GeV  $^3\text{He} + ^{197}\text{Au}$ . The primary differences between the ISiS ex-

perimental arrangement and that with the FASA array used in Ref. [25] are (1) in the ISiS, all fragments are  $Z$  and energy identified (including discrete He/Li separation), whereas this is only true for 0.4% of  $4\pi$  in the FASA array; (2) resolving times are  $\leq 300$  ns with ISiS, but much longer with the FASA array; (3) detector granularity is three times larger in ISiS (i.e., one-third the solid angle acceptance per detector); (4) maximum tolerable beam currents of  $\leq 1 \times 10^8/\text{spill}$  where employed in the present experiment; the studies in Ref. [25] used intensities of about  $5 \times 10^8$ , with a shorter spill time, and (5) an active collimator system was used to monitor beam halo in the present work, while this was not the case in Ref. [25]. These data should also be compared with the 5 GeV  $^4\text{He} + ^{197}\text{Au}$  measurements of Ref. [8], where an IMF multiplicity of  $3.2 \pm 0.8$  was reported for events triggered on IMF's with  $Z \geq 10$ . However, this trigger condition preferentially selects high multiplicity events so that a somewhat higher average multiplicity value is expected for that measurement, relative to our global results.

## B. Source characteristics

In order to interpret multifragmentation observables, it is essential to understand the time scale and degree of equilibration involved in the disassembly process. In this section, the characteristics of the multifragment source are examined. One way of evaluating the degree of equilibration in a reaction, as well as determining the average source velocity, is through a rapidity analysis. Figure 4 shows the longitudinal versus transverse velocity plots ( $v_{\perp}$  vs  $v_{\parallel}$ ) along points of constant invariant cross section for carbon fragments. The plots were created by selecting approximately equally-spaced points in the IMF kinetic energy spectra from near the spectral peaks to the high energy tails of the spectra. Both  $N_{\text{IMF}}=1$  and 3 analyses are presented to illustrate the effect of collision violence. Correlations of excitation-energy-related observables with  $N_{\text{IMF}}$  [27] indicate about a factor of 3 increase in excitation energy between  $N_{\text{IMF}}=1$  and 3. These plots are representative of  $Z \geq 5$  IMF's emitted from 4.8 GeV  $^4\text{He} + ^{197}\text{Au}$  and 1.8, 3.6, and 4.8 GeV  $^4\text{He} + \text{natAg}$  reactions. For  $Z \leq 4$ , a significant nonequilibrium component appears along the positive  $v_{\parallel}$  axis.

For an isotropically emitting source, the points of invariant cross section should fall on a locus centered at the laboratory velocity of the source. The lines in Fig. 4 are fits to the data for a constant value of invariant cross section in the  $(v_{\perp}, v_{\parallel})$  plane. To a good approximation, the data for a given invariant cross section are isotropic; i.e., they can be described by a circle with fixed locus, corresponding to a single average source velocity that increases with fragment kinetic energy. This suggests that the system is at least in “kinetic equilibrium” prior to fragment emission. We define “kinetic equilibrium” to mean that the momentum distribution of the source nucleons is chaotic, but may not necessarily have reached full statistical equilibrium. Comparable results are obtained for all systems; insufficient statistics were available for a rapidity analysis of the 1.8 GeV  $^3\text{He} + ^{197}\text{Au}$  system. Similar results have been noted in previous inclusive studies with  $^3\text{He}$  ions [9]. The source velocities (Table II) for all systems are  $\sim 0.01 - 0.02 c$  and are consistent with intranuclear cascade model predictions for the residues formed in

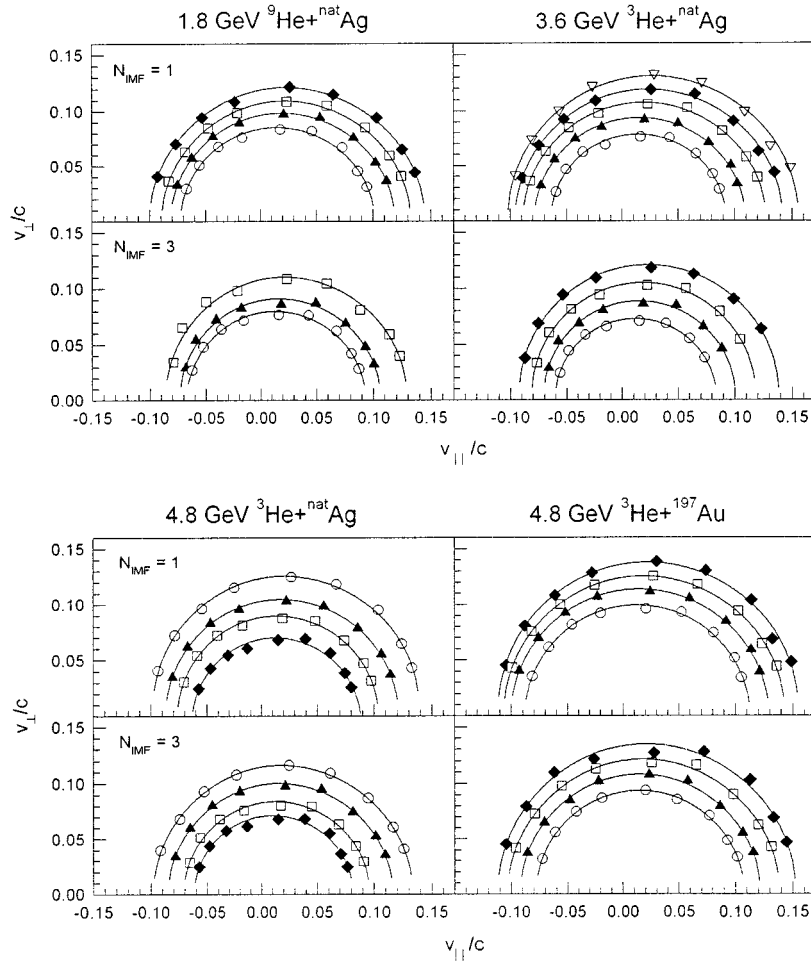


FIG. 4. Invariant cross sections,  $(1/p)d^2\sigma/dE d\Omega$ , for carbon fragments produced in the 4.8 GeV  ${}^3\text{He}+{}^{197}\text{Au}$  and 1.8, 3.6, and 4.8 GeV  ${}^3\text{He}+{}^{\text{nat}}\text{Ag}$  reactions. Top frames: fragments gated on  $N_{\text{IMF}}=1$ . Bottom frames: fragments gated on  $N_{\text{IMF}}=3$ .

these reactions [42]. The low source velocities, combined with the nearly isotropic emission pattern, suggested that the energy dissipation process involves a large transverse-momentum transfer in order to achieve the high excitation energies needed to produce the observed fragment multiplicities.

One trend that appears in the rapidity plots is that the source velocity increases almost linearly with velocity of the emitted IMF, as has been reported previously [43,44] for inclusive spectra. This suggests that as the fragment energy increases, there is a growing admixture of a faster source in the distribution of residues. Such a fast source is observed in the rapidity plots for lighter IMF's, such as Li and Be (not shown) and is necessary to obtain satisfactory fits in the moving-source analysis. Although the source velocities are consistent with the values reported in Ref. [9] in the 3.6 GeV  ${}^3\text{He}+{}^{\text{nat}}\text{Ag}$  reaction, the present work does not confirm the conclusion that the source velocity is independent of  $M_{\text{IMF}}$ , as reported in that work. The differences may be due to the higher solid angle coverage of the current experiment ( $\sim 69\%$  of  $4\pi$  for IMF's as comparable to  $\sim 8\%$  for Ref. [9]). In addition, the earlier data were taken at only three detector polar angles, two of which were near  $90^\circ$ ; thus that experiment was less sensitive to source velocity. Also, the present data are a better sample of  $N_{\text{IMF}}=3$  events, whereas

TABLE II. Source velocities ( $\beta = v/c$ ) extracted from rapidity plots. The first column of each set  $\langle\beta_{\text{IMF}}\rangle$  is the radius of the circles in Fig. 4. Source velocities are representative of an average source.

System	$N_{\text{IMF}}=1$		$N_{\text{IMF}}=3$	
	$\langle\beta_{\text{IMF}}\rangle$	$\langle\beta_{\text{source}}\rangle$	$\langle\beta_{\text{IMF}}\rangle$	$\langle\beta_{\text{source}}\rangle$
1.8 GeV ${}^3\text{He}+{}^{\text{nat}}\text{Ag}$	0.087	0.014	0.080	0.013
	0.100	0.019	0.090	0.016
	0.113	0.022	0.107	0.021
	0.129	0.022		
3.6 GeV ${}^3\text{He}+{}^{\text{nat}}\text{Ag}$	0.078	0.014	0.072	0.012
	0.094	0.015	0.086	0.015
	0.108	0.019	0.096	0.018
	0.119	0.023	0.115	0.023
	0.128	0.027		
4.8 GeV ${}^3\text{He}+{}^{\text{nat}}\text{Ag}$	0.076	0.012	0.072	0.010
	0.090	0.013	0.083	0.012
	0.104	0.017	0.100	0.016
	0.118	0.020	0.115	0.018
4.8 GeV ${}^3\text{He}+{}^{197}\text{Au}$	0.101	0.012	0.093	0.015
	0.115	0.014	0.107	0.015
	0.125	0.018	0.121	0.018
	0.133	0.022	0.132	0.020

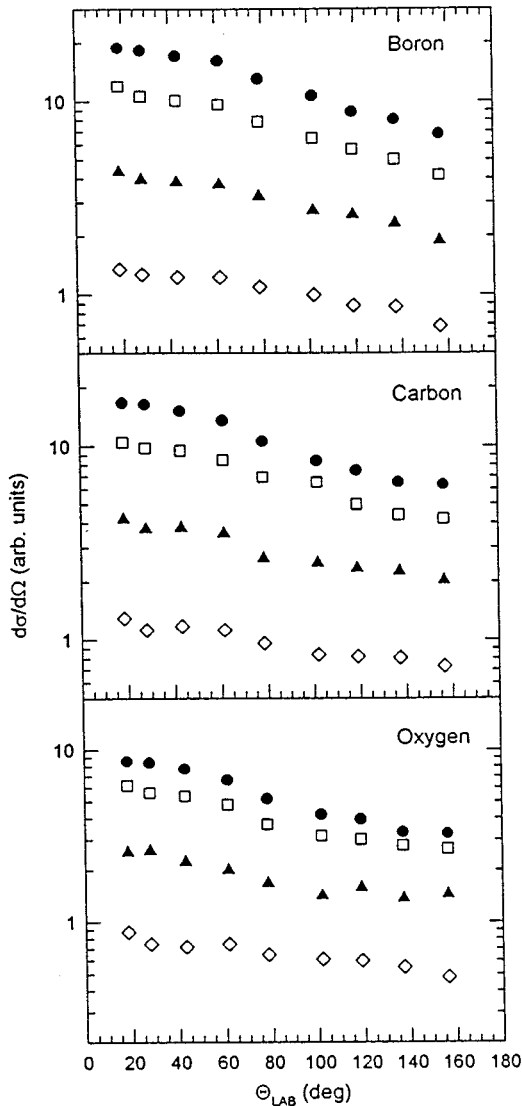


FIG. 5. Angular distributions for boron, carbon, and oxygen fragments emitted in the 4.8 GeV  ${}^3\text{He} + {}^{197}\text{Au}$  reaction, gated on total observed charge. Gating conditions are indicated on figure.

the former data represent an average over several higher multiplicities.

An isotropic source should also result in angular distributions that are symmetric about  $90^\circ$  in the source frame. In Fig. 5, the laboratory angular distributions for the 4.8 GeV  ${}^3\text{He} + {}^{197}\text{Au}$  reaction are shown for B, C, and O fragments, gated on total observed charge  $Z_{\text{obs}}$  in the event. These results are representative of all five systems measured in this work. As a general trend, the angular distributions do not change appreciably as a function of IMF charge for  $5 \geq Z < 11$ ; however, for lower  $Z$  values, the forward-angle yields are enhanced. The forward-backward asymmetry depends on deposition energy, with somewhat more isotropic behavior being observed for large values of  $Z_{\text{obs}}$ . For the highest  $Z_{\text{obs}}$  bins, the forward-backward ratios are consistent with isotropic emission in the center-of-mass frame from a source moving with velocities  $\sim 0.01\text{--}0.02c$ . The larger anisotropies observed for lower  $Z_{\text{obs}}$  values again suggests that presence of a forward-peaked nonequilibrium compo-

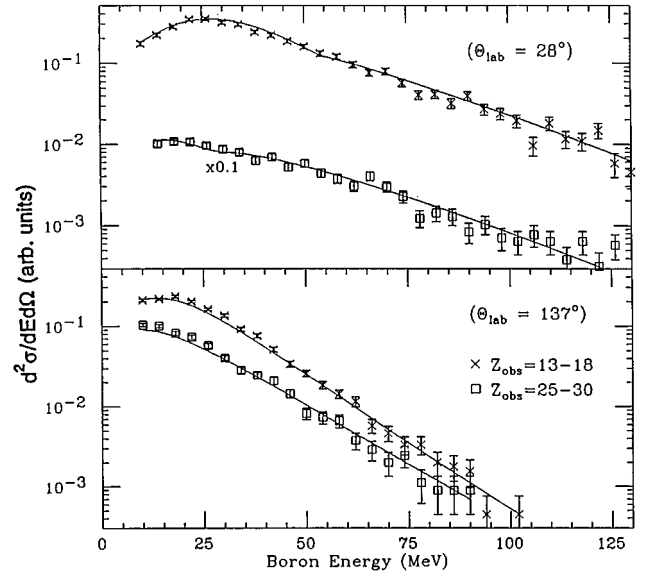


FIG. 6. Energy spectra for boron fragments emitted at  $28^\circ$  (top) and  $137^\circ$  (bottom) in the 4.8 GeV  ${}^3\text{He} + \text{natAg}$  reaction. Gating conditions on  $Z_{\text{obs}}$  are given in the key. Solid lines are two-component moving-source fits to the data [47].

nent in these data [27]. Analysis of the forward-backward character of the angular distributions shows little evidence for angular momentum effects.

In Figs. 6 and 7, the kinetic energy spectra of boron fragments emitted at  $28^\circ$  and  $137^\circ$  are shown for the 4.8 GeV  ${}^3\text{He} + {}^{197}\text{Au}$  and  $\text{natAg}$  systems, respectively. The gating conditions on total observed charge,  $Z_{\text{obs}}$ , are indicated on the figures. With increasing collision violence (higher  $Z_{\text{obs}}$ ), the spectral peak energy decreases, the peaks broaden toward lower energies, and a systematic hardening of the high energy spectral slopes evolves. A similar evolution is

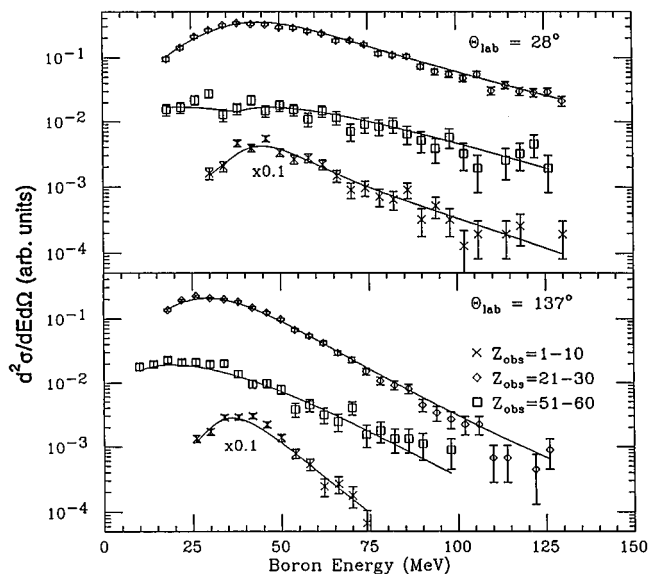


FIG. 7. Energy spectra for boron fragments emitted at  $28^\circ$  (top) and  $137^\circ$  (bottom) in the 4.8 GeV  ${}^3\text{He} + {}^{197}\text{Au}$  reaction. Gating conditions on  $Z_{\text{obs}}$  are given in the key. Solid lines are two-component moving-source fits to the data [47].

observed when gating on  $N_{\text{IMF}}$ , or other gauges of collision violence. The evolution of the spectral peaks to lower energies may be indicative of fragment emission from a dilute/expanding system [9,28,45]. In this context, the hardening of the spectral tails may result from a velocity boost of fragments emitted early in the expansion process [2].

In order to investigate the spectral shapes further, a moving source analysis [33,46,47] has been performed for IMF's as a function of  $Z_{\text{obs}}$ . The fits assumed that two sources are sufficient to account for most of the features present in the data when gated on  $Z_{\text{obs}}$ . The dominant (slow) source parametrization is based on the conditional saddle-point model of Moretto [48] and is approximately Maxwellian in form for light fragments, evolving toward a Gaussian function for heavier fragments:

$$d^3\sigma/dE d\Omega dz \propto f(Z_{\text{source}}, \beta, T, p, k_C). \quad (3)$$

Here  $Z_{\text{source}}$  is the charge of the source emitting a fragment of charge  $Z$ ;  $\beta$  is the source velocity;  $T$  is a slope-temperature parameter;  $p$  is a spectral shape parameter, and  $k_C$  is the fractional Coulomb repulsion energy, with  $k_C=1$  representing the Coulomb energy of touching spheres at normal nuclear matter density with  $r_0=1.2$  fm. The amplification parameter  $p$  is introduced to allow for possible variation in the Coulomb barrier due to the temperature and nonspherical shape of the emitting residue. An important aspect of these fits is that the charge of the emitting source is taken as  $Z_{\text{source}} = Z_{\text{target}} + Z_{\text{proj}} + Z_{\text{IMF}} - Z_{\text{obs}}$ ; i.e., it is assumed that all charge observed in the reaction is emitted *prior to* emission of the IMF. This assumption is equivalent to treating the emission as the last step in a sequential decay mechanism. While this is an extreme assumption, it minimizes the calculated Coulomb repulsion between the residue and the fragment by reducing the source charge in the fitting procedure. That is, the source radius derived from this procedure is a minimum, corresponding to a maximum value of the density.

The two-source parametrization includes a second fast source to account for nonequilibrium emission. The fast source was treated similar to the equilibrium parametrization of Eq. (2); however, the amplification parameter  $p$  was set to a constant value of 0.1 This fixes the shape of the nonequilibrium component to resemble a Maxwellian function. Both sources contain appropriate kinematic transformation from the moving frame to the laboratory system and the fit allows for recoil corrections. Inclusion of the second source is necessary to account for the change in spectral slopes observed for the low- $Z$  IMF's, especially lithium and beryllium. Contributions from the fast/nonequilibrium source decrease relative to the dominant source with increasing fragment charge and with increasing  $Z_{\text{obs}}$ . Hence, for boron and heavier fragments, a single source is sufficient to describe the dominant spectral features due to the relatively weak contribution of heavier IMF's to the fast source. Overall, the fast source accounts for about 15% of events containing one or more IMF's. Fits to the spectra at all angles were performed simultaneously, assuming isotropic distributions in the source frame of reference.

The best-fit parameters for a single source are shown in Table III for carbon fragments from the 4.8 GeV  $^3\text{He} + ^{197}\text{Ag}$ ,  $^{197}\text{Au}$  reactions. Values of reduced  $\chi^2/(\text{degree of}$

TABLE III. Moving-source fit parameters for carbon fragments, assuming a single source, tabulated as a function of  $Z_{\text{obs}}$ , from Ref [28]. Source parameters are representative of an average source. Bin sizes in  $Z_{\text{obs}}$  were chosen to give approximately the same fraction of total available charge for each target.

4.8 GeV $^3\text{He} + ^{197}\text{Au}$				
$Z_{\text{obs}}$	$\beta$	$k_C$	$T$	$p$
1–10	0.007	0.64	8.3	12.6
11–20	0.13	0.58	11.0	22.8
21–30	0.018	0.46	14.4	27.2
31–40	0.018	0.42	15.9	30.2
41–50	0.016	0.44	17.5	26.0
51–60	0.013	0.44	18.8	17.3
4.8 GeV $^3\text{He} + ^{\text{nat}}\text{Ag}$				
$Z_{\text{obs}}$	$\beta$	$k_C$	$T$	$p$
7–12	0.013	0.32	11.5	11.9
13–18	0.017	0.10	14.5	11.4
19–24	0.018	0.03	16.5	3.9
25–30	0.015	0.00	17.9	0.0
31–36	0.012	0.05	20.1	2.2

freedom) $\approx 3$  are obtained in these fits. Direct evidence for emission from an extended source is found in the behavior of the fractional Coulomb barriers  $k_C$  in Table III [28]. With increasing  $Z_{\text{obs}}$  values,  $k_C$  initially decreases as a function of increasing collision violence and then becomes constant, suggesting that once a sufficiently high degree of excitation is achieved, the system disintegrates. In order to obtain an estimate of the breakup density for the  $^{197}\text{Au}$  system, we compare values of  $k_C$  for the two extreme cases of  $Z_{\text{obs}}$ . The lowest bin ( $Z_{\text{obs}}=1-10$ ) should approximate emission from a source at normal nuclear matter density and the higher bins ( $Z_{\text{obs}}>31$ ) from the extended source. This analysis yields a value of  $\rho/\rho_0 \leq 1/3$  for the multifragmenting system.

The above observation, plus the apparent isotropic nature of the source (Fig. 4), is suggestive of significant energy deposition followed by nuclear expansion prior to multifragmentation of the system—or of some comparable mechanism that involves significant dilution of the Coulomb field of the emitting source. For example, the central-collision reaction trajectory plotted in Fig. 1 indicates that the residue enters the region of liquid-gas coexistence ( $\rho \sim 0.6\rho_0$ ) after about 40 fm/c. Subsequent cooling at constant entropy per baryon leads the system into the spinodal region at densities comparable to  $\rho/\rho_0 \sim 1/3$ . In addition, the geometry of the emitting source may also play an important role in a more quantitative analysis. The BUU calculations also predict that at the times of the order of 30–50 fm/c, there is significant density depletion in the center of the nucleus due to the removal of fast-cascade nucleus. This leaves a cavity in the central region of the nucleus that, given the presence of fluctuations, would serve to destabilize the system.

The source velocities in Table III agree with those obtained in the rapidity analysis and with predictions of INC calculations [19]. The source velocities initially rise and then fall with increasing  $Z_{\text{obs}}$ . The slope-temperature parameter,  $T$ , increases uniformly as a function of collision violence (observed charge), reaching a maximum near  $T \approx 18$  MeV.

For the least violent collisions (low  $Z_{\text{obs}}$ ), the inverse slopes of the spectral tails (temperature parameter) are relatively low, comparable to nonequilibrium emission in lower energy  ${}^3\text{He}$ -induced reactions [33]. This suggests that these events—about 15% of the total IMF yield—may be associated with nonequilibrium IMF's, perhaps from coalescence during the fast cascade step.

### C. Event-shape analysis

Determination of the time scale for disassembly of highly excited nuclei is central to understanding the mechanism for multifragment emission. Various models have been proposed to describe the time evolution of these processes, ranging from a time-ordered sequence of statistical binary decays to instantaneous breakup into several fragments (reviewed in Refs. [16] and [17]). A convenient distinction between these two extremes requires that the time interval between sequential decays be sufficiently long for the emitted fragment to escape the Coulomb field of the source.

One method of distinguishing between sequential and simultaneous fragment emission is to examine the spatial pattern of the ejectiles [49,50]. Simultaneous disassembly should produce a spherical event shape, whereas sequential binary decay should lead to a more elongated (needlelike) pattern. The event shape analysis prescribed by López, Fai, and Randrup [49,51] has been applied to the present data at 4.8 GeV bombarding energy. This procedure defines two quantities: sphericity ( $S$ ) and coplanarity ( $C$ ), which are combinations of the eigenvalues of the kinematic flow tensors constructed from the momentum components of the emitted particles [51]. In this context, a purely spherical event has unit sphericity ( $S=1.0$ ) and zero coplanarity; for pure sequential decay, the sphericity approaches zero.

The sphericity/coplanarity event-shape analysis of the present data at 4.8 GeV bombarding energy is summarized in Table IV. Because finite number effects can limit this technique [52], we have performed the analysis for two cases: (1) IMF's only and (2) all charged particles with energies below  $E/A \leq 8$  MeV. Inclusion of the larger ejectile set enhances the value of the sphericity. The values for the  ${}^3\text{He} + {}^{\text{nat}}\text{Ag}$  case are in general agreement with those of Cebra [53] for a symmetric system of about the same total mass ( $\langle S \rangle \approx 0.30$  and  $\langle C \rangle \approx 0.14$ ). The present sphericity results are significantly lower than reported in Ref. [9], where limited solid angle coverage was available and only the higher multiplicity events were examined. Figure 8 shows the evolution of the average sphericity  $\langle S \rangle$ , for combined LCP and IMF emission as a function of IMF multiplicity for the 4.8 GeV systems. The sphericity increases approximately linearly with observed IMF multiplicity, suggesting that simultaneous emission becomes more probable with increasing excitation energy; or, in the context of a sequential emission pattern, the time between successive steps becomes systematically shorter. Average coplanarity remains nearly constant ( $\leq 0.15$ ) as a function of IMF multiplicity for both systems.

In Table IV, the sphericity/coplanarity results are also compared with predictions of the simultaneous microcanonical multifragmentation calculation FREESCO [51] for each of the two ejectile sets, filtered through the detector geometry. The agreement is generally good. Thus, this limited analysis

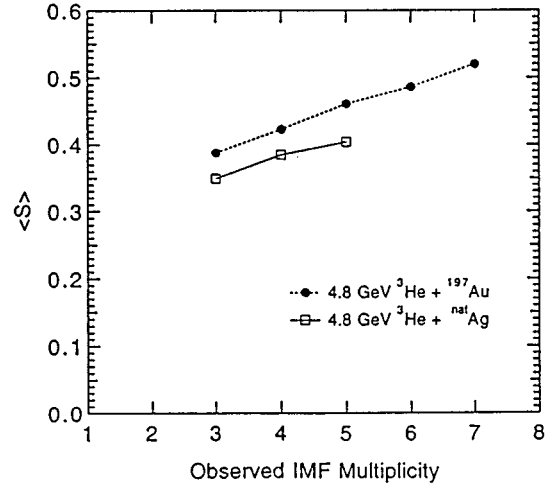


FIG. 8. Average sphericity,  $\langle S \rangle$ , for combined LCP and IMF emission, as a function of observed IMF multiplicity for the 4.8 GeV  ${}^3\text{He} + {}^{197}\text{Au}$ ,  ${}^{\text{nat}}\text{Ag}$  reactions, as indicated in the figure.

favors a simultaneous disassembly process; however, it is also consistent with a time-dependent picture in which fragments are emitted sequentially early in the reaction time, followed by subsequent simultaneous disintegration of the system at longer times.

### D. Charge distributions

In inclusive studies of proton-induced [45,54–56] and heavy-ion-induced reactions [57,58], it was found that the mass and charge distributions of IMF's exhibited a power law behavior. Values of the power-law exponent,  $\tau$ , are found to range from about 2 for systems that exhibit thermal-like properties to near 4 for nonequilibrium ejectiles [9,32,33,54–58]. Since fragment size distributions may reflect important features of the breakup dynamics [56–58], it is important to investigate the systematic features of such data. Unlike inclusive experiments, which average over contributions from many sources, the charge distributions from  $4\pi$  coincidence experiments can be examined as a function of observables that are linked to excitation energy. In this section, the evolution of IMF charge distributions as a function of observed IMF multiplicity, total observed charged-particle multiplicity, total observed charge, and total thermalized energy are discussed. The cluster charge distributions can be approximately described by a power law,

$$d\sigma/dZ \propto Z^{-\tau}, \quad (4)$$

TABLE IV. Event-shape parameters (sphericity= $S$  and coplanarity= $C$ ) for experimental data at 4.8 GeV and for events generated with FREESCO [51]. Data include all IMF multiplicities. Figure 8 shows dependence of  $S$  and  $C$  on multiplicity.

	${}^{\text{nat}}\text{Ag}$		${}^{197}\text{Au}$	
	$S$	$C$	$S$	$C$
IMF's (data)	0.24	0.12	0.28	0.13
IMF's (FREESCO)	0.18	0.10	0.27	0.10
LCP+IMF (data)	0.35	0.14	0.40	0.15
LCP+IMF (FREESCO)	0.38	0.15	0.50	0.15

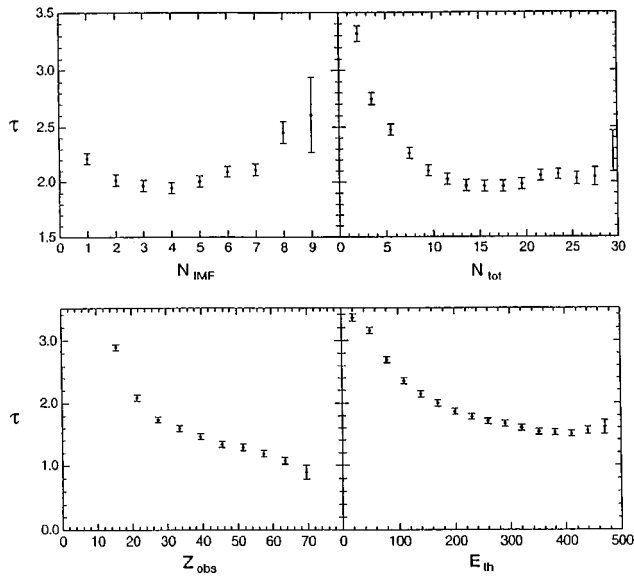


FIG. 9. The power-law exponent  $\tau$  as a function of IMF multiplicity ( $N_{\text{IMF}}$ ), total charged particle multiplicity ( $N_{\text{tot}}$ ), total observed charge ( $Z_{\text{obs}}$ ), and total thermal energy ( $E_{\text{th}}$ ) for 4.8 GeV  ${}^3\text{He} + {}^{197}\text{Au}$  system.

where  $Z$  is fragment charge. The  $\tau$  parameters for the 4.8 GeV  ${}^3\text{He} + {}^{197}\text{Au}$  system were determined by fitting Eq. (4) to the raw charge distributions for  $Z=3, 5-10$  and are presented in Fig. 9 as a function of IMF multiplicity,  $N_{\text{IMF}}$ ; total charged-particle multiplicity,  $N_{\text{tot}}$ ; the total observed charge,  $Z_{\text{obs}}$ , and the total thermalized energy,  $E_{\text{th}}$ . Beryllium was not included in the fits because particle-unstable  ${}^8\text{Be}$  is expected to be a major contributor to the yield. In all cases presented here, the fits were applied to the raw IMF distributions; i.e., no attempt was made to separate contributions from a fast/nonequilibrium source or to correct for detector thresholds. (This is investigated in Ref. [47].)

In Fig. 9, the 4.8 GeV  ${}^3\text{He} + {}^{197}\text{Au}$  system exhibits a decrease in the value of  $\tau$  above  $N_{\text{IMF}} > 1$  and reaches a minimum around  $\tau \approx 1.9$  for  $N_{\text{IMF}} \approx 4$  and then increases again with increasing IMF multiplicity. Thus there is an indication that for large values of  $N_{\text{IMF}}$ , the production of heavy fragments becomes less favorable. The values of  $\tau$  as a function of the total observed charged-particle multiplicity,  $N_{\text{tot}}$ , also decrease from about 3.3 for  $N_{\text{tot}} \approx 2$  down to a minimum near  $\tau \approx 1.9$  for  $N_{\text{tot}} \approx 15$ . It is observed that the ratios of H to He also exhibit minima consistent with the minima observed in  $\tau$  as a function of both  $N_{\text{IMF}}$  and  $N_{\text{tot}}$ . The minima in  $\tau$  values as a function of both  $N_{\text{IMF}}$  and  $N_{\text{tot}}$ , as well as the minimum observed for the H/He ratios, may be understood in terms of the conservation of total charge available for fragmentation. As noted earlier, IMF multiplicity is correlated with excitation energy. At lower excitation energies, where IMF emission resembles an evaporative process, emission of lighter IMF's (and therefore higher  $\tau$  values) is favored because of the dominant role of the Coulomb barrier. As the excitation energy increases, thermal expansion may lead to lower effective Coulomb barriers, increasing the probability of emitting heavier fragments, as discussed in the next section. At energies near the total binding energy, increasing excitation energy will begin to favor the formation

of smaller clusters and thus inhibit the formation of heavier fragments, leading to higher  $\tau$  values.

In contrast, no minima are observed when  $\tau$  values are plotted as a function of total observed charge  $Z_{\text{obs}}$ , and total thermalized energy,  $E_{\text{th}}$ , for the  ${}^3\text{He} + {}^{197}\text{Au}$  system. When examined as a function of  $Z_{\text{obs}}$ , a steep decrease in  $\tau$  values is observed, from  $\tau \sim 10$  at low  $Z_{\text{tot}}$  down to  $\tau \sim 2$  at  $Z_{\text{tot}} = 20$ , followed by a more gradual decrease with  $Z_{\text{obs}}$  that extends down to  $\tau \leq 1$ . When interpreting the most violent events, it is important to recognize that  $Z_{\text{obs}}$  and  $\tau$  are highly correlated. Hence the results may be biased towards events with large multiplicities (large  $\tau$ ) or with large fragment charges (low  $\tau$ ). For the systems studied here, the fragment charges seem to play a more dominant role. The values of  $\tau$  as a function of the total thermalized energy,  $E_{\text{th}}$ , seem to be midway between the trends for  $N_{\text{tot}}$  and  $Z_{\text{tot}}$ ; the  $\tau$  values decrease from  $\tau \sim 3.5$  at low total thermalized energy. Above observed values of  $E_{\text{th}} \approx 200$  MeV (corresponding to an excitation energy of about 600 MeV), the  $\tau$  values remain relatively constant near  $\tau \sim 1.5$ . This result suggests that once a sufficiently high excitation of the system is attained, the charge distributions become insensitive to further excitation.

It is apparent from the above discussion that the evolution of the charge distributions is sensitive to the correlation observable. Careful analysis (in which detector thresholds and contributions from fast and slow sources are carefully evaluated) is necessary to interpret such distributions in terms of the breakup dynamics. Further, higher moments of the charge distributions need to be explored [59].

### III. HYBRID MODEL COMPARISONS

In this section, the multifragmentation data are compared with predictions of a hybrid intranuclear cascade (INC)/expanding emitting source (EES) model [2,19,42]. Excitation energy distributions from the INC calculations based on the ISABEL code [42], binned in 100 MeV steps along with the corresponding average values of the residue mass, charge and velocity of the residue, provide input for the expanding emitting source calculation [2]. The EES model stresses the time evolution of the emission process. It assumes statistical emission of fragments and treats expansion in terms of a giant monopole oscillation driven by thermal pressure. The binding energy of the instantaneous source follows a parabolic density dependence, governed by an effective compressibility parameter  $K$ . In these calculations,  $K = 144$  MeV was employed, based on previous analysis of the 3.6 GeV  ${}^3\text{He} + {}^{\text{nat}}\text{Ag}$  system [19]. For heavy-ion reactions, somewhat larger values of  $K$  provide a good description of the IMF multiplicity data [18]. A Fermi energy of 25 MeV was employed for the Ag target and 30 MeV for Au. Within the context of this model, initial particle emission occurs sequentially, but on a fast time scale ( $\leq 70$  fm/c) during the expansion. If the thermal pressure is sufficient to reach nuclear densities of  $\rho/\rho_0 \leq 0.3$ , instantaneous multifragmentation of the residue occurs. At this point, surface fragment emission is replaced by volume emission in calculating the fragment energy spectra. Volume emission may also be interpreted in terms of simultaneous breakup of the expanded residue.

The reconstructed IMF multiplicity distributions are com-

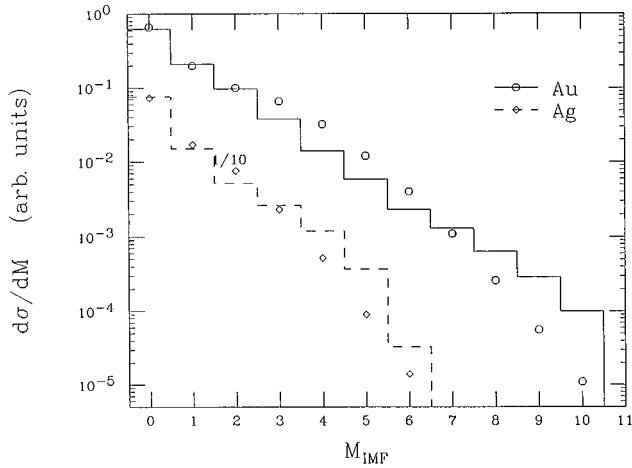


FIG. 10. IMF multiplicity distributions for the 4.8 GeV  ${}^3\text{He}+{}^{197}\text{Au}$ ,  ${}^{197}\text{Au}$  reactions. Points correspond to reconstructed experimental data; lines to the results of INC/EES calculations. Data for 3.6 GeV  ${}^3\text{He}+{}^{\text{nat}}\text{Ag}$  system are nearly identical to those at 4.8 GeV.

pared with the calculated results in Figs. 10 and 11. For  ${}^{197}\text{Au}$  at 4.8 GeV, the calculation describes the data well for most of the IMF cross section (Fig. 10). For  ${}^{\text{nat}}\text{Ag}$  at 3.6 and 4.8 GeV, where both experimental and theoretical results are nearly identical, the agreement is somewhat poorer, but could be improved by including detector thresholds in the simulation. Better agreement would also be obtained with a somewhat larger value of  $K$  (however, see below). In comparing the INC/EES model with the data for these two dissimilar targets no attempt has been made to adjust the input parameters, which are identical for both targets and based on those in Kwiatkowski *et al.* [19]. It is also possible that the residue excitation energies are being overpredicted by ISABEL due to selection of the fast rearrangement option [42]. Additionally, the initial density depletion that occurs during the fast cascade, as well as fluctuations in source size (within each excitation energy bin), are not taken into account and may influence the distributions. Overall, the calculations and

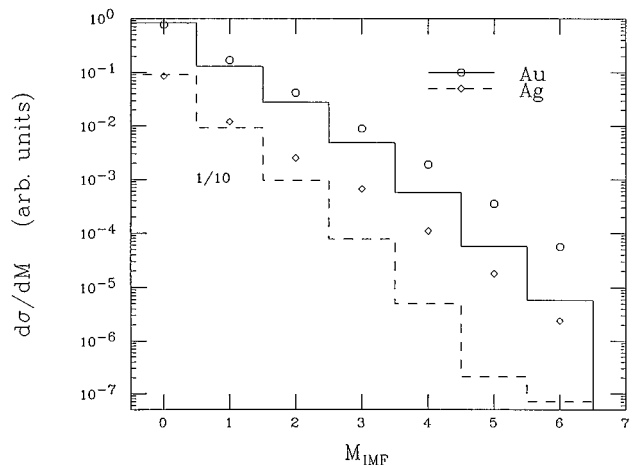


FIG. 11. IMF multiplicity distributions for the 1.8 GeV  ${}^3\text{He}+{}^{197}\text{Au}$ ,  ${}^{197}\text{Au}$  reactions. Points correspond to reconstructed experimental data; lines to the results of INC/EES calculations.

data are consistent only if expansion is included in the model, as the cross sections for higher IMF multiplicities are dramatically underpredicted for large values of  $K$ , as has been demonstrated for the 3.6 GeV  ${}^3\text{He}+{}^{\text{nat}}\text{Ag}$  system in Ref. [19]. In contrast, comparison of the INC/EES model for the two targets at 1.8 GeV is less satisfactory (Fig. 11). At this bombarding energy, a lower value of  $K$  would be required to obtain a better fit. However, in this case the proximity to the multifragmentation threshold makes the results much more sensitive to the distribution of excitation energies predicted by the INC code.

Predictions of the spectral shapes by the INC/EES model are compared with the data for carbon fragments in Fig. 12. The trends in the data and model parallel one another well; similar agreement is found for other charged fragments as well. The spectral peaks broaden and shift toward lower energy while the tails harden with increasing  $Z_{\text{obs}}$ . Particular success is achieved in reproducing the data for large  $Z_{\text{obs}}$  values, where the model should be most appropriate for comparison with the data. In terms of the model, the overall behavior can be explained as follows. The most energetic fragments are emitted early in the expansion from a high  $Z$  source near normal nuclear density; they also receive a kinematic boost from the source expansion from a high  $Z$  source near normal nuclear density; they also receive a kinematic boost from the source expansion velocity. Since both the excitation energy and expansion velocity should scale with  $Z_{\text{obs}}$ , the spectral slopes are expected to become systematically flatter with increasing  $Z_{\text{obs}}$ . For systems that expand to the critical breakup density ( $\rho/\rho_0 \leq 0.3$ ), the system is highly distended. Thus fragments emitted at this stage experience greatly reduced Coulomb repulsion, which is further influenced by the effects of volume emission with a random distribution of fragment velocities. This results in a broad kinetic energy distribution for the fragments.

Poorest agreement in Fig. 12 is found for the lower  $Z_{\text{obs}}$  bins, especially at forward angles. Fast (e.g., coalescence-like) processes [33,44] in more peripheral reactions may contribute to the experimental spectra; this mechanism is not included in the INC/EES model.

#### IV. SUMMARY AND CONCLUSIONS

The  ${}^3\text{He}+{}^{197}\text{Au}$ ,  ${}^{\text{nat}}\text{Ag}$  systems have been studied for bombarding energies between 1.8 and 4.8 GeV using the ISiS detector array in which fragments are  $Z$  identified over a substantial fraction of  $4\pi$  with good granularity.

The highest IMF multiplicities were observed in the 4.8 GeV  ${}^3\text{He}+{}^{197}\text{Au}$  reaction, with an average reconstructed IMF multiplicity of  $\langle M_{\text{IMF}} \rangle = 2.0$  for events in which at least one IMF was detected. This value is similar to those observed in heavy-ion reactions for similar total mass and total bombarding energy [39–41], but much lower than the value of 3.8 previously reported by Lips *et al.* [25] for the comparable 4.0 GeV  ${}^4\text{He}+{}^{197}\text{Au}$  reaction.

Evidence that at least ‘‘kinetic equilibrium’’ of the system is achieved before fragmentation takes place is found in the results of rapidity and moving-source analyses. The low source velocities derived from the data imply that substantial transverse momentum is imparted to the nucleus in the collision. In addition, these analyses provide evidence for a fast

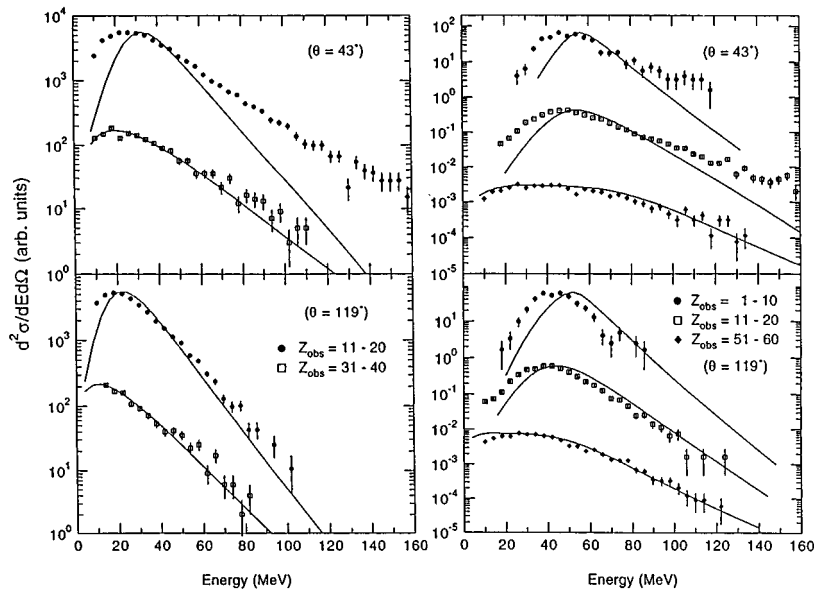


FIG. 12. Left: Laboratory energy spectra of carbon fragments for 4.8 GeV  ${}^3\text{He} + {}^{\text{nat}}\text{Ag}$  reactions at  $43^\circ$  and  $119^\circ$ . Points correspond to experimental data; lines to the results of INC/EES calculations. Gating conditions on  $Z_{\text{obs}}$  are given in the key. Right: Laboratory energy spectra of carbon fragments for 4.8 GeV  ${}^3\text{He} + {}^{197}\text{Au}$  reactions at  $43^\circ$  and  $119^\circ$ . Points correspond to experimental data; lines to the results of INC/EES calculations. Gating conditions on  $Z_{\text{obs}}$  are given in the key.

source that contributes about 15% to the IMF yield. An event-shape analysis of 4.8 GeV  ${}^3\text{He} + {}^{\text{nat}}\text{Ag}$ ,  ${}^{197}\text{Au}$  reactions yields sphericity values consistent with the simultaneous emission code FREESCO [51].

One of the strongest pieces of evidence for fragment emission from an extended source with  $\rho < \rho_0$  is obtained from moving-source fits to the fragment energy spectra [28,47]. The low fractional Coulomb-barrier parameters extracted from these fits support this interpretation, independent of any theoretical model, and correspond to a breakup density of  $\rho/\rho_0 \lesssim 1/3$ . The fits also exhibit an increase in the slope-temperature parameter from approximately 8 to 18 MeV over the range of total observed charge, indicating a hardening of the spectral tails with increasing collision violence.

An analysis of IMF charge distributions as a function of several observables believed to be related to the residue excitation energy shows that the charge distributions evolve differently, depending on the observable. A minimum in the power-law parameter  $\tau$  is observed as a function of IMF multiplicity and total charged-particle multiplicity for the 4.8 GeV  ${}^3\text{He}$  bombardments on both targets. This implies that initially the probability for heavy fragment emission increases with increasing excitation energy, reaches a maximum and then decreases again at the highest excitation energies. However, the charge distributions become increasingly flat with increasing total observed charge and thermalized energy. The different trends in the evolution of the charge distributions illustrate that interpretation of such results is linked to the choice of excitation energy gauge.

Comparisons of the data to the intranuclear cascade/expanding emitting source (INC/EES) hybrid model [19] show qualitative agreement for the 4.8 GeV multiplicity data on both targets. The agreement is less satisfactory at 1.8 GeV bombarding energy, where threshold effects are more impor-

tant. In either case, if thermal expansion is excluded from the hybrid model calculation (i.e., emission is from a source at normal nuclear density), the cross sections for high IMF multiplicity events are dramatically underpredicted for both targets at all energies.

Further success of the INC/EES model is found in the description of the evolution of the fragment kinetic energy spectra as a function of observed charge. For the spectra, the most probable energy decreases while the width of the spectral peak increases and the tails become flatter with increasing violence (higher observed charge) of the collision. In the context of the model, the broadening of the spectral peaks towards lower kinetic energies is due to volume emission from a dilute source ( $\rho < \rho_0$ ). Similarly, the slope of the high-energy tails of the spectra become harder as a consequence of a boosting of fragment velocity by the expansion of the source. Thus the success of the model in simultaneously fitting the IMF multiplicity distributions and energy spectra for highly dissipative events argues in favor of an evolutionary reaction mechanism in which rapid sequential emission occurs during nuclear expansion, followed by simultaneous breakup of the system at low densities (or some mechanism involving significant perturbation of the nuclear Coulomb field).

#### ACKNOWLEDGMENTS

The authors thank B. Serot, H. Müller, S. Pratt, P. Danielewicz, W. Bauer, and A. Botvina for valuable discussions concerning multifragmentation phenomena. We also acknowledge the technical staff of DAPNIA/CE Saclay, as well as J. Arvieux and the staff at LNS for their support in making these experiments possible; in particular, G. Milleret for his assistance with the beam optics. Among the numerous

others who contributed to the success of this project were F. Haroutel, A. Mansion, J. Faure, J. C. Lugol and his staff, J. P. Passerieux, C. Mazur, K. McDonald, T. Hamilton, C. Powell, G. Wang, D. Ginger, and Z. Fraenkel. We also acknowledge the financial support of the U.S. Department of

Energy; additional support was provided by Indiana University, Commissariat à l'Énergie Atomique (France), the U.S. National Science Foundation, the National Science and Energy Research Council (Canada), NATO, and KBN Grant No. 0719/P3/93/04 (Poland).

- 
- [1] J. P. Bondorf, R. Donangelo, I. N. Mishustin, C. J. Pethick, H. Schulz, and K. Sneppen, *Nucl. Phys.* **A443**, 321 (1985); **A436**, 265 (1985).
- [2] W. A. Friedman, *Phys. Rev. C* **42**, 667 (1990); in *Towards a Unified Picture of Nuclear Dynamics*, AIP Conf. Proc. No. 250, edited by F. Sakata (AIP, New York, 1991), p. 422.
- [3] D. H. E. Gross, *Rep. Prog. Phys.* **53**, 605 (1990); D. H. E. Gross and R. Heck, *Phys. Lett. B* **318**, 405 (1993).
- [4] J. Randrup and S. E. Koonin, *Nucl. Phys.* **A356**, 223 (1981).
- [5] H. Müller and B. D. Serot, *Phys. Rev. C* **52**, 2072 (1995); B. D. Serot and J. D. Walecka, *Adv. Nucl. Phys.* **16**, 1 (1986).
- [6] S. Pratt, *Phys. Rev. A* **42**, 1447 (1990).
- [7] T. J. Schlagel and V. R. Pandharipande, *Phys. Rev. C* **36**, 162 (1987).
- [8] A. I. Warwick, H. H. Wieman, H. H. Gutbrod, M. R. Maier, J. Peter, H. Stelzer, and F. Welk, *Phys. Rev. C* **27**, 1083 (1983).
- [9] S. J. Yennello *et al.*, *Phys. Rev. Lett.* **67**, 671 (1991); *Phys. Rev. C* **48**, 1092 (1993).
- [10] D. R. Bowman *et al.*, *Phys. Rev. Lett.* **67**, 1527 (1991).
- [11] J. Pochodzalla *et al.*, *Phys. Rev. Lett.* **75**, 1040 (1995); J. Hubele *et al.*, *Z. Phys. A* **340**, 263 (1991).
- [12] J. Natowitz *et al.*, *Nucl. Phys.* **A538**, 263c (1992).
- [13] J. Peter *et al.*, *Nucl. Phys.* **A538**, 75c (1992).
- [14] B. Jakobsson *et al.*, *Nucl. Phys.* **A509**, 195 (1990).
- [15] G. Rusch, W. Heinrich, B. Wiegel, E. Winkel, and J. Dreute, *Phys. Rev. C* **49**, 901 (1994).
- [16] W. G. Lynch, *Annu. Rev. Nucl. Part. Sci.* **37**, 439 (1987).
- [17] L. G. Moretto and G. J. Wozniak, *Annu. Rev. Nucl. Part. Sci.* **43**, 379 (1993).
- [18] R. T. deSouza *et al.*, *Phys. Lett. B* **268**, 6 (1991).
- [19] K. Kwiatkowski, W. A. Friedman, L. W. Woo, V. E. Viola, E. C. Pollacco, C. Volant, and S. J. Yennello, *Phys. Rev. C* **49**, 1516 (1994).
- [20] Bao-an Li, A. R. De Angelis, and D. H. E. Gross, *Phys. Lett. B* **303**, 225 (1993).
- [21] R. Wolfgang, E. W. Baker, A. A. Caretto, J. B. Cumming, G. Friedlander, and J. Hudis, *Phys. Rev.* **103**, 394 (1956).
- [22] J. Cugnon, D. Kinet, and J. Vandermuelen, *Nucl. Phys.* **A379**, 553 (1982); **A462**, 751 (1987).
- [23] P. Danielewicz, *Phys. Rev. C* **51**, 716 (1995).
- [24] G. Wang, K. Kwiatkowski, V. E. Viola, W. Bauer, and Danielewicz, *Phys. Rev. C* **53**, 1811 (1996).
- [25] V. Lips *et al.*, *Phys. Rev. Lett.* **72**, 1604 (1994).
- [26] K. Kwiatkowski *et al.*, *Nucl. Instrum. Methods A* **360**, 571 (1995).
- [27] K. B. Morley *et al.*, preceding paper, *Phys. Rev. C* **54**, 737 (1996).
- [28] K. Kwiatkowski *et al.*, *Phys. Rev. Lett.* **74**, 3756 (1995).
- [29] G. Friedlander, J. M. Miller, R. Wolfgang, J. Hudis, and E. Baker, *Phys. Rev.* **94**, 727 (1954).
- [30] V. P. Crespo, J. M. Alexander, and E. K. Hyde, *Phys. Rev.* **131**, 1765 (1963); R. G. Korteling and E. K. Hyde, *ibid.* **136**, 425 (1964).
- [31] N. A. Perfilov, O. V. Lozhkin, and V. P. Samov, *Sov. Phys. Usp.* **3**, 1 (1960).
- [32] A. Hirsch *et al.*, *Phys. Rev. C* **29**, 508 (1984).
- [33] K. Kwiatkowski, J. Bashkin, H. Karwowski, M. Fatyga, and V. E. Viola, *Phys. Rev. B* **171**, 41 (1986).
- [34] P. Kozma *et al.*, *Nucl. Instrum. Methods A* **291**, 662 (1990).
- [35] H. Quéchon, Ph.D. thesis, Université Paris Sud, Orsay, 1980.
- [36] S. Kox *et al.*, *Nucl. Phys.* **420**, 162 (1984).
- [37] P. Karol, *Phys. Rev.* **11**, 1203 (1975).
- [38] J. Hudis, in *Nuclear Chemistry*, edited by L. Yaffe (Academic, New York, 1968), p. 169.
- [39] D. R. Bowman *et al.*, *Phys. Rev. C* **46**, 1834 (1992).
- [40] L. Phair *et al.*, *Phys. Rev. B* **285**, 10 (1992).
- [41] F. Saint-Laurent *et al.*, *Nucl. Phys.* **A583**, 481 (1995).
- [42] Y. Yariv and Z. Fraenkel, *Phys. Rev. C* **24**, 488 (1981).
- [43] P. B. Price and J. Stevenson, *Phys. Lett.* **78B**, 197 (1978).
- [44] R. E. L. Green, R. G. Korteling, and K. P. Jackson, *Phys. Rev. C* **29**, 1806 (1984).
- [45] A. M. Poskanzer, G. W. Butler, and E. K. Hyde, *Phys. Rev. C* **3**, 882 (1971); **3**, 882 (1971).
- [46] G. D. Westfall, R. G. Sextro, A. M. Poskanzer, A. M. Zebelman, G. W. Butler, and E. K. Hyde, *Phys. Rev. C* **17**, 1368 (1978).
- [47] D. Bracken, Ph.D. thesis, Indiana University, 1995.
- [48] L. G. Moretto, *Nucl. Phys.* **A247**, 211 (1975).
- [49] J. A. López and J. Randrup, *Nucl. Phys.* **A491**, 477 (1989).
- [50] W. Gawlikowicz and K. Grotowski, *Nucl. Phys.* **A551**, 73 (1993).
- [51] G. Fai and J. Randrup, *Nucl. Phys.* **A404**, 551 (1983); G. Fai and J. Randrup, *Comput. Phys. Commun.* **42**, 385 (1986).
- [52] J. P. Bondorf, C. H. Dasso, R. Donangelo, and G. Pollarollo, *Phys. Lett. B* **240**, 28 (1990).
- [53] D. Cebra *et al.*, *Phys. Rev. Lett.* **64**, 1246 (1990).
- [54] J. E. Finn *et al.*, *Phys. Rev. Lett.* **49**, 1321 (1982).
- [55] R. E. L. Green and R. G. Korteling, *Phys. Rev. C* **22**, 1594 (1980).
- [56] N. T. Porile *et al.*, *Phys. Rev. C* **39**, 1914 (1989).
- [57] A. D. Panagiotou, M. W. Curtin, H. Toki, D. K. Scott, and P. J. Siemens, *Phys. Rev. Lett.* **52**, 496 (1984).
- [58] J. L. Wile *et al.*, *Phys. Rev. C* **45**, 2300 (1992).
- [59] M. L. Gilkes *et al.*, *Phys. Rev. Lett.* **73**, 1590 (1994).